

# A Misalignment Tolerant Inductive Power Transfer System With AC Resistance Reduction

Weihao Zhao<sup>1</sup>, Zhan Shen<sup>2</sup>, *Member, IEEE*, Yingzhou Peng<sup>3</sup>, *Member, IEEE*,  
and Huai Wang<sup>4</sup>, *Senior Member, IEEE*

**Abstract**—Misalignment sensitivity is one of the main problems limiting the development of inductive power transfer system. When misalignment occurs, the system output power and efficiency reduce dramatically and cause unstable power supply. Meanwhile, the ac resistance of the inductive power transfer coil increases with the frequency. In medium and high frequency region, it produces large ohmic loss and thermal dissipation, which lead to efficiency-drop and temperature-rise problems. This work proposes a misalignment-tolerant winding pattern to reduce the system horizontal misalignment sensitivity, thermal stress, and coil ac resistance. From the experimental result, the proposed winding pattern reduces the ac resistance maximally by 88% at 2 MHz compared with the conventional winding pattern under the same geometry and wire type. The misalignment tolerance is maximally improved by 46% in terms of the output power with the proposed winding pattern.

**Index Terms**—AC resistance, coupling coefficient, inductive power transfer (IPT), misalignment tolerance, litz-wire planar coils.

## I. INTRODUCTION

IN RECENT years, inductive power transfer (IPT) systems are gradually used in low-power consumer electronics, biomedical implants to high-power electric vehicle (EV) chargers [1], [2], [3].

However, the development of IPT systems in industrial applications is slow and mainly limited by three challenges. They are misalignment sensitivity, low efficiency, and excessive thermal dissipation [4], [5]. During the daily operation, the misalignment between the transmitter and receiver may occur and reduce the system efficiency and power transfer stability. In some high-power applications, e.g., EV and industrial robot charger, the transmitter and receiver coils conduct high current

at medium frequency according to standard SAE J2954 [6]. When the medium-frequency and high-amplitude current flows through the coils, the large ac resistance produces ohmic loss and increases the coil temperature due to Joule effect. It results in more investment in the cooling system design and thermal-management difficulty. In biomedical and consumer electronic applications, the transmitter and receiver coils operate at hundreds of kilohertz (kHz) or even megahertz (MHz) range [2], [3]. The misalignment sensitivity and temperature-rise problems due to the ac resistance are more pronounced. They could lead to bad user experience, and even be harmful to biomedical implant patients.

In order to solve the misalignment-sensitivity issues, researchers proposed different methods from the control aspect, resonant tank structure aspect to coil design aspect [7], [8], [9], [10], [11], [12], [13], [14], [15], [16], [17]. In [8], an unsymmetrical coil pair was proposed. The transmitter is a solenoid coil with a smaller area and the receiver is a planar coil with a wider area than the transmitter. The misalignment tolerance is improved by increasing the geometry difference between the transmitter and receiver. The authors in [14] and [15] proposed a magnetic integrated compensation coil design method to improve the misalignment tolerance and power transfer capacity. The authors in [16] proposed a hybrid array resonator structure to create a uniform magnetic field and improve the misalignment tolerance. Xu et al. [17] used the genetic algorithm to optimize the coil structure and reduce the misalignment sensitivity. Lee et al. [12] used an interoperable coil to improve the misalignment tolerance. The double D coil was proposed in [11], which increased the misalignment tolerance by enlarging the charging zone and creating a uniform magnetic field distribution. The authors in [7] and [13] used one extra coil in the center of the transmitter or receiver to cancel the mutual inductance variation, and improve the misalignment tolerance. However, these solutions require more material to construct the transmitter and receiver, which increases the material usage and ac resistance, and potentially induces thermal management problems for coils. In some volume-critical applications, e.g., biomedical implants, enlarging the coil size is not feasible.

The existing solutions increase the misalignment tolerance mainly by changing the coil geometry and using multiple transmitter or receiver coils. This work proposes a misalignment-tolerant winding pattern to reduce the ac resistance and thermal stress of the coil without changing the coil geometry and number of coils. A comparison between the existing solutions and this

Manuscript received 8 June 2023; revised 19 August 2023 and 6 September 2023; accepted 26 September 2023. (Corresponding authors: Weihao Zhao; Shen Zhan; Yingzhou Peng.)

Weihao Zhao and Huai Wang are with the AAU Energy, Aalborg University, 9220 Aalborg, Denmark (e-mail: wzh@energy.aau.dk; hwa@energy.aau.dk).

Zhan Shen is with the Southeast University, Nanjing 211189, China (e-mail: zhs@seu.edu.cn).

Yingzhou Peng is with the Hunan University, Changsha 410082, China (e-mail: yzpeng@hnu.edu.cn).

Color versions of one or more figures in this article are available at <https://doi.org/10.1109/TIE.2023.3321981>.

Digital Object Identifier 10.1109/TIE.2023.3321981

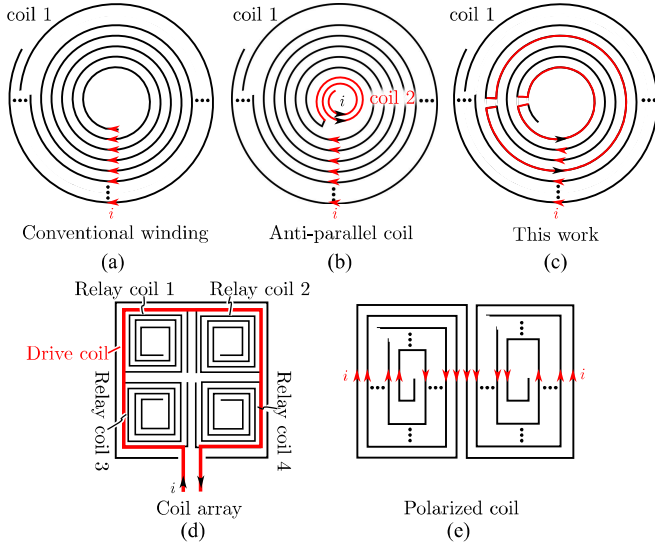


Fig. 1. Comparison between (a) conventional winding, (b) antiparallel coil [7], [13], and (c) this work, (d) coil array [16], (e) polarized coil [11].

work regarding the coil structure is presented in Fig. 1. The conventional winding pattern connects each turn of the coil in series. The authors in [7] and [13] added the antiparallel coil in the center of the receiver or transmitter coil. The proposed winding pattern alternates the winding direction to make a semi-homogeneous magnetic field, which enhances the misalignment tolerance. The coil array structure utilize more coils to create a large and uniform magnetic field [16]. The polarized coil structure changes the magnetic field direction to horizontal direction, and enlarges the charging area. The difference between this work and [7], [13], and [16] is as follows.

- 1) The authors in [7], [13], and [16] used multiple coils to minimize the coupling factor variation. These approaches increase the material cost and ac resistance. This work reduces the coupling factor variation by alternating the winding direction, which does not need extra coils. From the cost and winding loss perspective, the proposed method can improve the misalignment tolerance without significantly increasing the material usage and ac resistance compared with [7] and [13].
- 2) Compared with the conventional coil, [7], [13], and [16] changed the coil structure on coil level. However, this work only changes the coil structure on turn level. From the complexity and coil structure perspective, the proposed method is simpler than [7] and [13].
- 3) This work considers the opposite-turn effects on the misalignment sensitivity, ac resistance, and inductance, which are neglected in [7], [13], [16].

To date, using Litz wire with a smaller strand diameter is the main solution to minimize the coil ac resistance at medium and high frequency region. Due to the manufacturing difficulty, Litz wire with thinner strands is more expensive and less common on the market. In this work, the proposed winding pattern can reduce the ac resistance without changing the Litz wire type

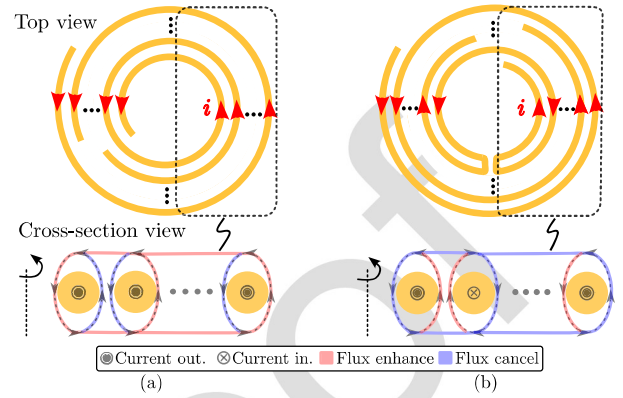


Fig. 2. Top and cross-section view of planar spiral coils with magnetic flux distribution for (a) conventional winding pattern and (b) proposed winding pattern.

and material usage. Comparing with the existing literature, the contribution of this study is as follows.

- 1) A cost-effective method is proposed to reduce the ac resistance and thermal stress of coils, and improve the misalignment tolerance.
- 2) Changing the winding pattern and arranging different winding directions are a new design freedom. It is first proposed in this work.
- 3) A design method is proposed to find the suitable position to allocate the opposite winding direction, which results in high misalignment tolerance.

The rest of this article is organized as follows. Section II presents a misalignment-tolerant winding pattern and compares it with the conventional winding patterns in terms of the magnetic field distribution, ac resistance, coupling factor and quality factor. The reason why the proposed winding pattern results in lower ac resistance and higher misalignment tolerance is detailed with theoretical analysis and numerical simulation results. In Section III, prototypes with the proposed and conventional winding patterns are compared in terms of the ac resistance, inductance, coupling factor, and output power. A design method is proposed to find the suitable reversed winding position, which results in high misalignment tolerance. Finally, Section IV concludes the article.

## II. WINDING PATTERN OF PLANAR COILS

### A. Theoretical Analysis

A comparison between the proposed winding pattern and conventional winding pattern is presented in Fig. 2 with different magnetic flux distribution. The conventional winding pattern connects each turn in series and has the same current direction between each turn. The magnetic flux from outer turns is added into the inner turns, which results in more steep magnetic field distributions as shown in Figs. 2(a) and 3(a). The proposed winding pattern connects each turn in series but alternates the winding direction. The same current-direction turns enhance the magnetic field intensity, but the opposite current-direction turns cancel the magnetic field intensity. By properly alternating the

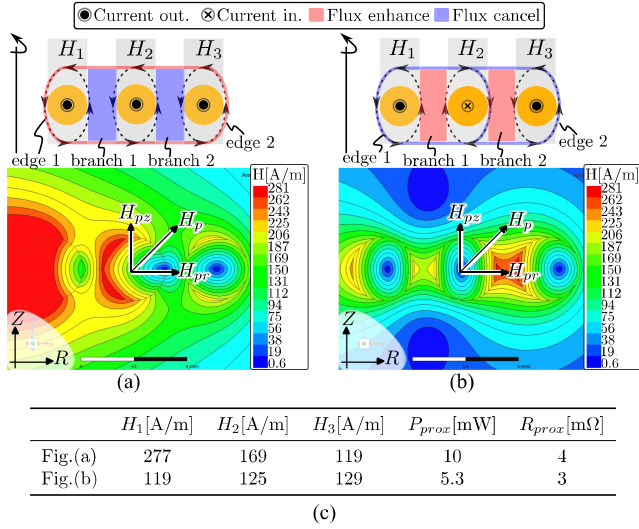


Fig. 3. Three-turn planar coil made with (a) conventional winding pattern, (b) proposed winding pattern, and (c) magnetic field intensity and proximity-effect power loss comparison.

winding direction, a uniform magnetic field can be created with the proposed winding pattern. It is visualized in Figs. 2(b) and 3(b). According to [16] and [17], the uniform magnetic field is beneficial to enhance the misalignment tolerance.

The proximity-effect power loss is affected by magnetic field intensity [18]

$$P_{prox} = G_r H_e^2$$

$$G_r = \frac{-2\pi\gamma \operatorname{ber}_2\gamma \operatorname{ber}'\gamma + \operatorname{bei}_2\gamma \operatorname{bei}'\gamma}{\sigma \operatorname{ber}^2\gamma + \operatorname{bei}^2\gamma} \quad \gamma = \frac{d}{\sqrt{2}\delta} \quad (1)$$

where  $P_{prox}$  is the unit length proximity-effect power loss.  $H_e$  is the peak value of the external magnetic field.  $d$ ,  $\delta$ , and  $\sigma$  are the wire diameter, skin depth, and conductivity of the conductor.  $\operatorname{ber}$ ,  $\operatorname{bei}$  are Kelvin functions, and  $\operatorname{ber}'$ ,  $\operatorname{bei}'$  are the corresponding derivatives.

Since the conventional winding pattern enhances the magnetic field intensity between each turn as shown in Fig. 3(a), it creates a larger proximity-effect power loss. In comparison, the opposite winding directions in the proposed winding pattern reduce the magnetic field intensity as shown in Fig. 3(b). Therefore, a lower proximity-effect power loss can be achieved according to (1).

A three-turn coil is used as an example and shown in Fig. 3. The magnetic field intensity of the first, second, and third turns are denoted by  $H_1$ ,  $H_2$ , and  $H_3$ . They are calculated by the surface integral of point magnetic field intensity  $H_p$

$$H_i = \iint_{s_i} H_p ds \quad i \in 1, 2, 3 \quad (2)$$

where  $s_i$  is the area of  $i_{th}$  turn. The point magnetic field intensity is decomposed on the radial and axial directions

$$H_p = \sqrt{H_{pr}^2 + H_{pz}^2} \quad (3)$$

where  $H_{pr}$  and  $H_{pz}$  are the radial and axial components of point magnetic field intensity. For the conventional winding pattern in

Fig. 3(a), the radial point magnetic field intensity is

$$H_{pr} = H_{r,1} + H_{r,2} + H_{r,3} \quad (4)$$

where  $H_{r,i}$  is the radial magnetic field intensity of  $i_{th}$  turn. The axial point magnetic field intensity at the branch 1 and 2 are

$$H_{pz,branch1} = H_{z,1} - H_{z,2} - H_{z,3}$$

$$H_{pz,branch2} = H_{z,1} + H_{z,2} - H_{z,3} \quad (5)$$

where  $H_{pz,branch1}$ ,  $H_{pz,branch2}$  are the axial point magnetic field intensity at branches 1 and 2.  $H_{z,i}$  are the axial magnetic field intensity of the  $i_{th}$  turn. The axial point magnetic field intensity at the edge 1 and 2 are as follows:

$$H_{pz,edge1} = -H_{z,1} - H_{z,2} - H_{z,3}$$

$$H_{pz,edge2} = H_{z,1} + H_{z,2} + H_{z,3}. \quad (6)$$

For the proposed winding pattern in Fig. 3(b), the second turn has the opposite current direction, and produces the reverse magnetic field. The radial magnetic field is

$$H_{pr} = H_{r,1} - H_{r,2} + H_{r,3}. \quad (7)$$

On the axial direction, the magnetic field intensity at the branch 1 and 2 are

$$H_{pz,branch1} = H_{z,1} + H_{z,2} - H_{z,3}$$

$$H_{pz,branch2} = H_{z,1} - H_{z,2} - H_{z,3}. \quad (8)$$

The axial magnetic field intensity at the edge 1 and 2 are

$$H_{pz,edge1} = -H_{z,1} + H_{z,2} - H_{z,3}$$

$$H_{pz,edge2} = H_{z,1} - H_{z,2} + H_{z,3}. \quad (9)$$

The radial and axial magnetic field intensity are calculated by [19]. The relevant equations are given in the Appendix VI. Substituting (2) ~ (9) to (1), the proximity-effect power loss and resistance are obtained

$$P_{prox} = G_r \iint_{s_i} H_{pr}^2 + H_{pz}^2 ds$$

$$R_{prox} = \frac{2P_{prox}}{I^2} \quad (10)$$

where  $I$  is the current amplitude. The calculated proximity-effect power loss and ac resistance are given in Fig. 3(c). In comparison, the proposed winding pattern reduces the magnetic field intensity surrounding the coil. Therefore, the corresponding proximity-effect power loss is reduced by 4.7 mW, which is 47% reduction compared with the conventional winding pattern. The proximity effect resistance is reduced by 1 mΩ, which is 25% relative ac resistance reduction.

## B. Numerical Simulation

In this section, three case studies are carried out with Maxwell 2D and 3D to prove that the misalignment tolerance can be improved with the proposed winding pattern. In case study one, the coupling factor variation and efficiency factor variation for conventional and proposed winding patterns are compared at different misalignment distance by Maxwell 3D. In case study two, the magnetic field distribution created by different winding



patterns are compared with an eight-turn planar coil example in Maxwell 2D. In case study three, the surface magnetic field and coupling factor of the proposed winding pattern and conventional winding pattern are compared at 85 kHz for EV applications with Maxwell 3D.

**1) Case Study 1:** A 16-turn planar coil is built in Maxwell 3D with 3 A, 500 kHz current excitation. The conventional winding pattern has the same winding direction between each turns. The proposed winding pattern has opposite winding directions in the fourth, eighth, and twelfth turn of the receiver. The antiparallel coil has opposite winding directions in the first, second, and third turn of the receiver. The coupling factor and its gradient are calculated by

$$k = \frac{M}{\sqrt{L_t L_r}} \quad \rho_k = \frac{\partial k}{\partial x} \Big|_{x=x_i, y_i} \quad (11)$$

where  $k$ ,  $\rho_k$  are the coupling factor and its gradient.  $M$ ,  $L_t$ , and  $L_r$  are the mutual inductance, transmitter and receiver self inductance.  $R_t$  and  $R_r$  are the transmitter and receiver resistance.  $x$  is the misalignment distance.

The efficiency factor and its gradient is calculated by

$$\eta = kQ = \frac{\omega M}{\sqrt{R_t R_r}} \quad \rho_e = \frac{\partial \eta}{\partial x} \Big|_{x=x_i, y_i} \quad (12)$$

where  $\eta$  and  $\rho_e$  are the efficiency factor and its gradient.  $Q$  is the quality factor.

When the transmitter and receiver coils are aligned, the conventional winding pattern has the highest efficiency factor and coupling factor, which are shown in Fig. 4(a) and (c). When misalignment happens, the efficiency factor and coupling factor of the conventional winding pattern decrease faster than the antiparallel winding pattern and proposed winding pattern. In Fig. 4(b) and (d), the proposed winding pattern has the lowest coupling factor and efficiency factor variation. It indicates that the proposed winding pattern has higher misalignment tolerance than conventional winding pattern and antiparallel winding pattern.

**2) Case Study 2:** An eight-turn planar coil example is built in Maxwell 2D with 3 A, 500 kHz current excitation. Since the uniform magnetic field can improve the misalignment tolerance [16], [17], four different winding patterns are compared in terms of the uniformity of magnetic field intensity, which is calculated as the gradient of the magnetic field intensity in Fig. 5. The winding direction of different winding patterns are represented by  $\odot$  and  $\otimes$  in Fig. 5.  $\odot$  denotes outward current direction and  $\otimes$  denotes the inward current direction.

The comparison between different winding patterns is given in Fig. 5(e). The conventional winding pattern and winding pattern one create the highest magnetic field intensity in the center of the coil, but it decreases dramatically along the horizontal direction. The winding pattern two and three create a more uniform magnetic field with low magnetic field intensity in the center of the coil. In comparison, conventional winding pattern can result in the highest coupling factor at the aligned condition, but it has the lowest misalignment tolerance. By reversing the winding direction, the magnetic field can be shaped into a semihomogeneous field with lower variation in the horizontal direction,

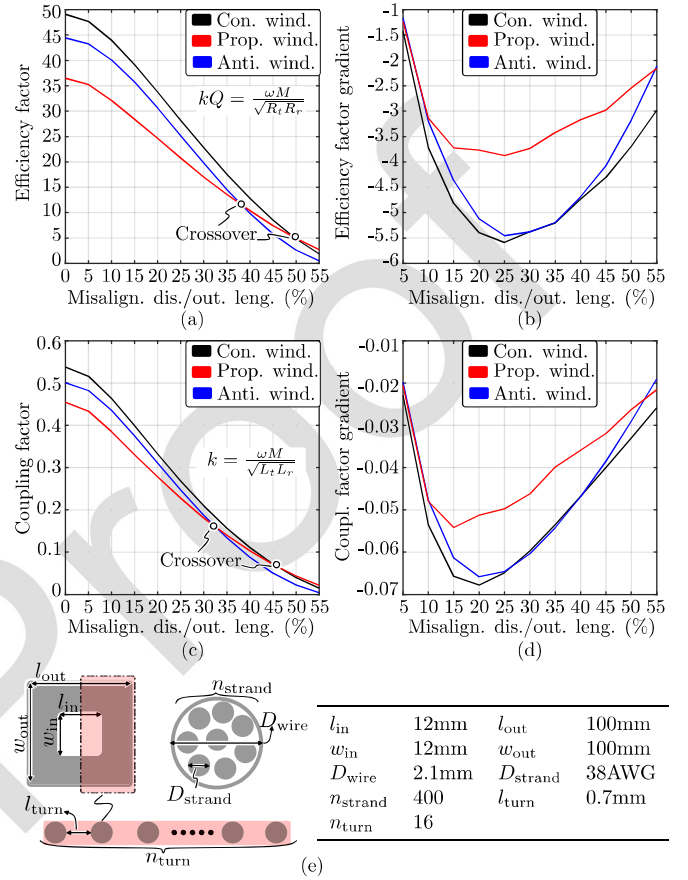


Fig. 4. Comparison between the conventional winding pattern, proposed winding pattern and antiparallel winding pattern in terms of (a) efficiency factor, (b) efficiency factor gradient, (c) coupling factor, (d) coupling factor gradient, and (e) detailed simulation parameters and coil geometry.

which indicates high misalignment tolerance. Since the position of the reversed winding direction affects the coupling factor variation and magnetic field distribution, a factor is proposed to evaluate the performance of different winding patterns

$$F = \sum_{i=1}^N \rho_{ki} \rho_{ei} \quad (13)$$

where  $\rho_{ei}$ ,  $\rho_{ki}$  are the efficiency factor gradient and coupling factor gradient at the  $i_{th}$  misalignment point.  $N$  is the number of misalignment points.  $F$  is the performance factor. A lower value of  $F$  indicates higher misalignment tolerance.

**3) Case Study 3:** In Fig. 6, a 16-turn coil example is built in Maxwell 3D with 20 A and 85 kHz current excitation according to SAE J2954 [6] for EV application. The model geometry information is given in Fig. 4(e). The proposed winding pattern reverses the current direction at the seventh, eighth, and ninth turn. From the top-side magnetic field comparison, the conventional-proposed coil pair generates a more uniform magnetic field than the conventional-conventional coil pair. From the cross-section view, the conventional-proposed coil pair has a lower magnitude of the magnetic field compared with the conventional-conventional coil pair. It indicates that

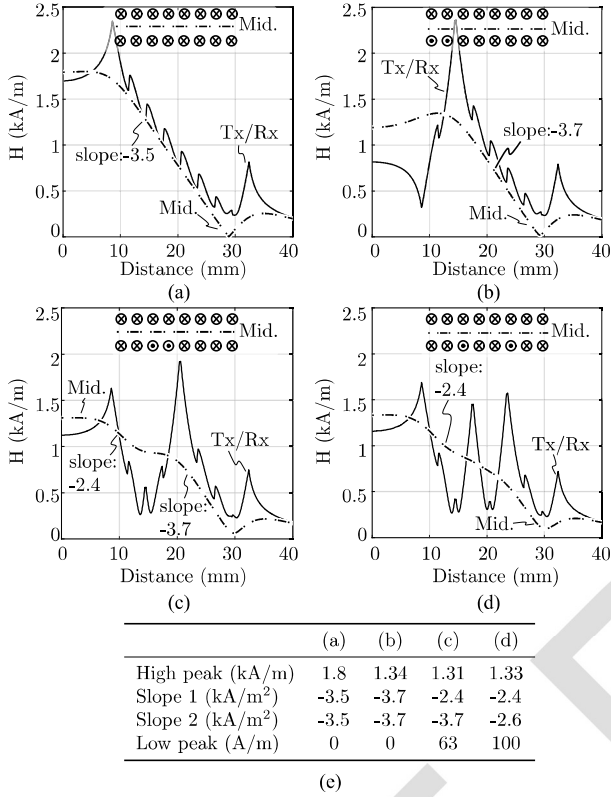


Fig. 5. Transmitter/receiver and middle line magnetic field distribution for (a) conventional winding pattern, (b) winding pattern one, (c) winding pattern two, (d) winding pattern three, and (e) magnetic field intensity magnitude and gradient comparison between different winding patterns at the middle line.

its coupling factor at the aligned condition is lower than that of the conventional-conventional coil pair. According to (10), the proposed-conventional coil pair has smaller proximity-effect resistance. When the relative misalignment distance is 40% larger than the coil outer length, the proposed-conventional coil pair has a higher coupling factor than the conventional-conventional coil pair.

### III. EXPERIMENTAL VERIFICATION

#### A. AC Resistance and Inductance Comparison

In order to verify that the ac resistance can be reduced by alternating the winding direction, four coils with conventional and proposed winding patterns are compared in Fig. 7. Their ac resistance are measured by high-precision impedance analyzer E4990 A with test fixture 16047E [20]. The ac resistance reduction is calculated by

$$|\Delta R| = R_{\text{con}} - R_{\text{prop}} \quad \Delta R = \frac{|\Delta R|}{R_{\text{prop}}} \quad (14)$$

where  $|\Delta R|$  is the absolute ac resistance reduction, and  $\Delta R$  is the relative ac resistance reduction.  $R_{\text{con}}$  is the ac resistance of coils made with the conventional winding pattern, and  $R_{\text{prop}}$  is the ac resistance of coils made with proposed winding pattern.

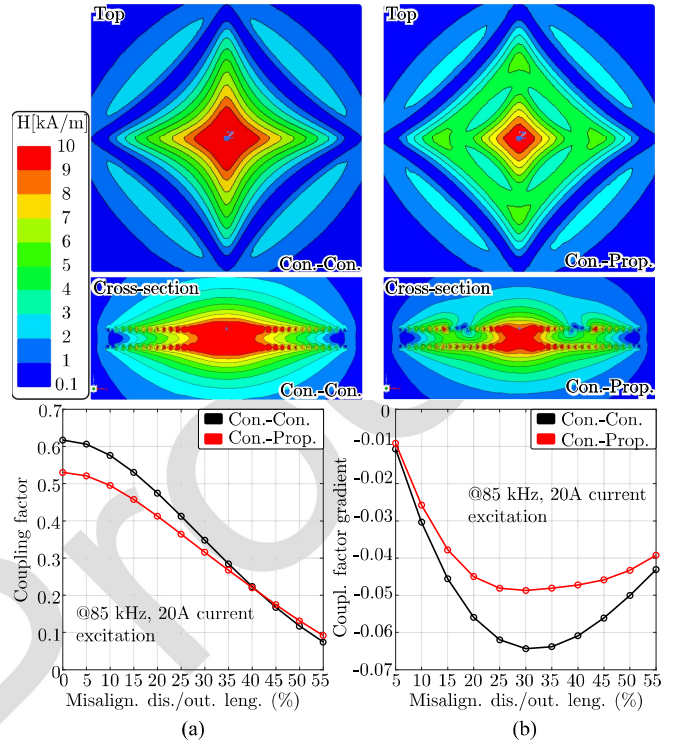


Fig. 6. Maxwell 3D simulation result for conventional-conventional and conventional-proposed coil pairs with (a) coupling factor and (b) its gradient comparison.

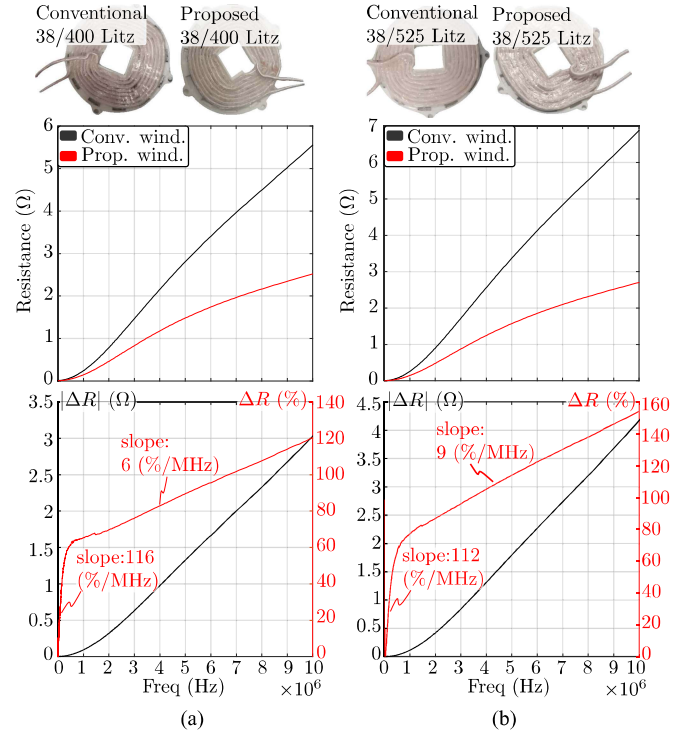


Fig. 7. Comparison between ac resistance of conventional and proposed winding pattern with relative and absolute ac resistance reduction for an eight-turn rectangular coil example with (a) 400 strands Litz wire and (b) 525 strands Litz wire.

In Fig. 7(a) and (b), the coils are made with 400 strands and 525 strands Litz wire with strand diameter of 38 AWG. With the same Litz wire but different winding pattern, the ac resistance is reduced by 70% at 2 MHz and 120% at 10 MHz for 38/400 Litz wire, and 88% at 2 MHz and 160% at 10 MHz for 38/525 Litz wire. According to (1) and (10), the frequency-dependent resistance is dependent on the magnetic field intensity surrounded by coil. From Figs. 3, 5, and 6, the proposed winding pattern can reduce the magnetic field intensity compared with the conventional winding pattern. Therefore, the proposed winding pattern can result in lower ac resistance compared with the conventional winding pattern as shown in Fig. 7.

With the same winding pattern but different Litz wire, the ac resistance for 38/525 Litz wire is lower than that for 38/400 Litz wire in low frequency region, but larger in high frequency region. In low frequency region, the 38/525 Litz wire has larger conduction area than 38/400 Litz wire. Therefore, its resistance is lower. As the 38/525 Litz wire has more strand number than the 38/400 Litz wire, its proximity effect is more pronounced than 38/400 Litz wire, which results in larger proximity-effect resistance in high frequency region [18].

In Fig. 7, the ac resistance reduction rates have two different slopes. When the frequency is below 700 kHz, the ac resistance reduction rate is increased with 116%/MHz for 400/38 AWG Litz wire, and 112%/MHz for 525/38 AWG Litz wire. This is because the proposed winding pattern can effectively reduce the turn-level proximity-effect ac resistance at below 700 kHz. When the frequency is above 700 kHz, which exceeds the optimal operating frequency for the selected Litz wire, the skin-effect resistance is more pronounced and cannot be canceled with the proposed winding pattern. Therefore, the ac resistance reduction rate is reduced in the high frequency region in Fig. 7.

Since the proposed winding pattern has reversed winding directions, which reduce the magnetic field intensity, it results in inductance reduction. Three combinations of different winding patterns are measured with impedance analyzer E4990 A and their inductance and coupling factors are presented in Fig. 8. When the receiver and transmitter are made with the conventional winding pattern, the leakage inductance from the transmitter and receiver are higher than their mutual inductance. It indicates that the majority part of the magnetic flux is not linking the transmitter and receiver. When the receiver is made with the proposed winding pattern and the transmitter is made with the conventional winding pattern, the mutual inductance is higher than the receiver leakage inductance, but lower than the transmitter leakage inductance. From the receiver perspective, the majority part of the magnetic flux links with the transmitter. When the receiver and transmitter are made with proposed winding pattern, the mutual inductance and leakage inductance are decreased. The mutual inductance is lower than the receiver and transmitter leakage inductance. It means that the proposed winding pattern needs more turn number in order to obtain the same amount of the mutual inductance as the convention winding pattern at aligned condition.

The coupling factor is calculated by (11), and presented in Fig. 8(d). The coupling factor is 0.45 when conventional winding

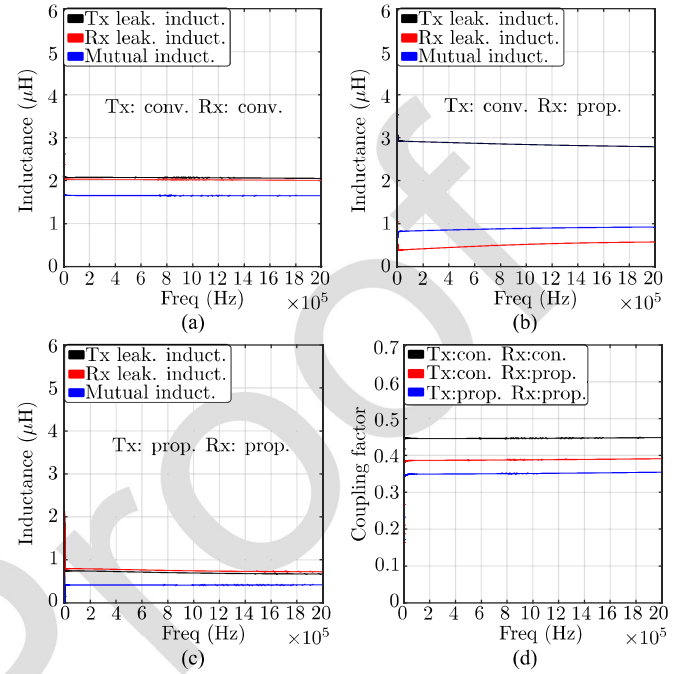


Fig. 8. Comparison between the inductance for (a) conventional-conventional coil pair, (b) conventional-proposed coil pair, (c) proposed-proposed coil pair, and (d) coupling factor.

pattern is used as the transmitter and receiver. It reduces to 0.39 when one of the coils is made with the conventional winding pattern and the other is made with the proposed winding pattern. It decreases to 0.35 when all coils are made with the proposed winding pattern.

By reversing the winding direction, the total magnetic field intensity is reduced, which decreases the ac resistance, inductance, and coupling factor. Since the reversed winding position affects the magnetic field distribution, ac resistance, inductance, and coupling factor, a design method is proposed in Fig. 9 to find the suitable reversed winding position, which guarantees high misalignment tolerance. Meanwhile, a design guideline is presented below to guide designers to find the suitable reversed winding direction.

- 1) Step 1: According to the application area and standards, designers can identify the operating frequency, e.g., 85 kHz for EV charger. Thereafter, the suitable strand size can be selected according to frequency chart in [21].
- 2) Step 2: According to the output power requirement, input and output voltage requirements, designers can estimate the current amplitude which flows through the coils. Based on the estimated value, designers should select the Litz wire, which has larger copper filling area than the required value. The minimum strand number is calculated according to

$$S_{\text{copper}} \leq 0.25\pi D_{\text{strand}}^2 n_{\text{strand}} \quad (15)$$

where  $S_{\text{copper}}$  is the minimum copper filling area.  $n_{\text{strand}}$  is the strand number and  $D_{\text{strand}}$  is the strand diameter obtained from step 1.



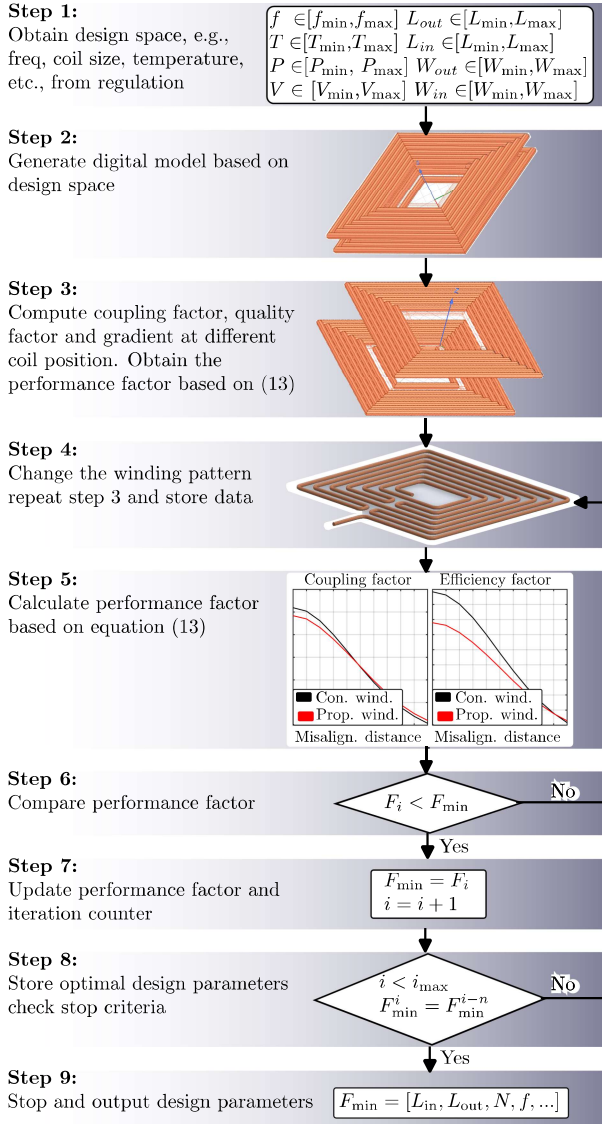


Fig. 9. Design flowchart for the proposed winding pattern.

- 3) Step 3: Based on the product availability, designers can select the suitable product and obtain the Litz wire parameters for simulation.
- 4) Step 4: Based on the size requirements, designers can estimate the maximum turn number of the coil according to

$$N_{\max} = \min \left\{ \frac{L_{\text{out}} - L_{\text{in}} - \rho_l}{2D_{\text{wire}}}, \frac{W_{\text{out}} - W_{\text{in}} - \rho_w}{2D_{\text{wire}}} \right\} \quad (16)$$

where  $N_{\max}$  is the maximum turn number.  $L_{\text{out}}, W_{\text{out}}$  are the maximum outer length and width.  $L_{\text{in}}, W_{\text{in}}$  are the minimum inner length and width.  $D_{\text{wire}}$  is the wire diameter obtained from the step 3.  $\rho_l, \rho_w$  are the tolerance factor to guarantee a feasible design.

- 5) Step 5: Based on the identified design space, designers can make digital models as the base case by using numerical simulation software and estimate the quality

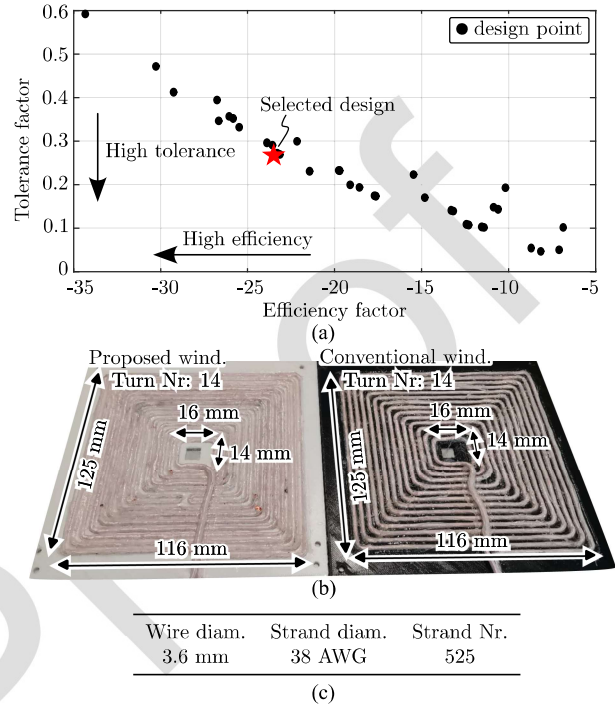


Fig. 10. (a) A 34-iteration example with the proposed design method for different reversed winding position, (b) design result for the proposed winding pattern and conventional winding pattern, and (c) Litz wire parameters.

- factor, coupling factor, and their gradients at different misalignment distance.
- 6) Step 6: Designers can sweep the different winding patterns, and calculate the coupling factor, quality factor and their gradient at different misalignment distance.
- 7) Step 7: The performance factor is calculated by (13) for the fifth and sixth step.
- 8) Step 8: The performance factor obtained from the seventh step is compared with the minimum performance factor obtained from previous iterations. If a smaller performance factor is found, it goes to the ninth step. Otherwise, another reversed winding combination is generated from the seventh step and evaluated.
- 9) Step 9: The minimum performance factor is updated and the iteration counter  $i$  is increased by one.
- 10) Step 10: The current iteration counter is compared with the maximum allowable iteration. If the iteration counter is greater or equal than the maximum allowable value, the design algorithm stops and outputs the optimal design parameters. If the minimum performance factor has remained unchanged over  $n$  consecutive iterations, the algorithm also stops and outputs the optimal design parameters.

By following the proposed design method, a 34-iteration example is presented in Fig. 10 with different reversed winding positions. The efficiency factor is calculated by (12), and the performance factor is calculated by (13). A negative sign is added to the efficiency factor in order to unify the optimization

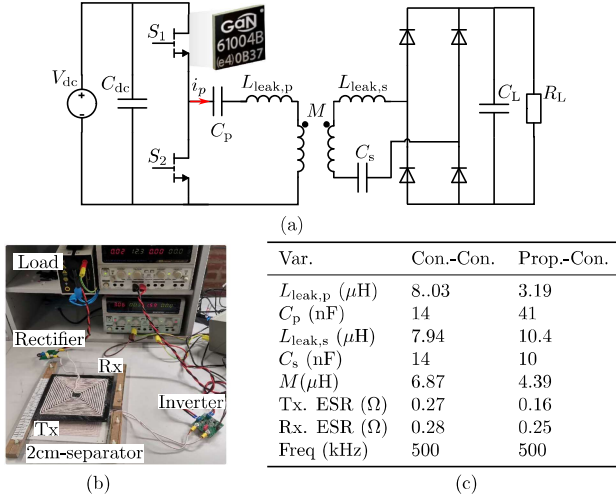


Fig. 11. (a) Series-series compensated topology, (b) measurement setup, and (c) resonant tank parameters.

direction (e.g., minimize both the efficiency and performance factors). A lower performance factor indicates a higher misalignment tolerance. However, there is a tradeoff between the efficiency and misalignment tolerance. The highest efficiency maybe obtained with the lowest misalignment tolerance, and the largest misalignment tolerance may result in the lowest efficiency. In this study, we chose the middle point in Fig. 10(a) to design the coil, which has moderate misalignment tolerance and efficiency. The design result is presented in Fig. 10(b).

### B. Misalignment Sensitivity Analysis

A 30-W IPT demonstrator is designed for powering consumer electronics. According to European telecommunication standard institute (ETSI) [22], the operating frequency is 500 kHz, which is frequency band four. Two different coil pairs are designed by following the design procedure. The coil geometry (i.e., inner length and width, outer length and width, and turn number), Litz wire type and wire length are controlled in the same amount. The detail parameters are given in Fig. 10(b) and (c). Therefore, the charging area and material cost are the same. The vertical separation distance between the transmitter and receiver is 2 cm.

In the first coil pair, the transmitter and receiver coils are wound with the conventional winding pattern. In the second coil pair, the transmitter has a reverse winding direction in the seventh and fourteenth turn and receiver is conventional winding pattern. It results in the semihomogeneous magnetic field distribution and high misalignment tolerance.

The topology of the demonstrator is presented in Fig. 11(a), and the test setup is presented in Fig. 11(b). The technical parameters are given in Fig. 11(c). The compensated capacitor is high-quality film capacitors with low ESR (i.e., 10 ~ 20 m  $\Omega$  at 500 kHz), and the capacitance is selected to compensate the leakage inductance and ensure the converter operating at the inductive region. Therefore, the zero-voltage-switching (ZVS) at 500 kHz is obtained to minimize the switching losses. The measured gate-source voltage,  $V_{gs}$ , drain-to-source voltage,  $V_{ds}$ ,

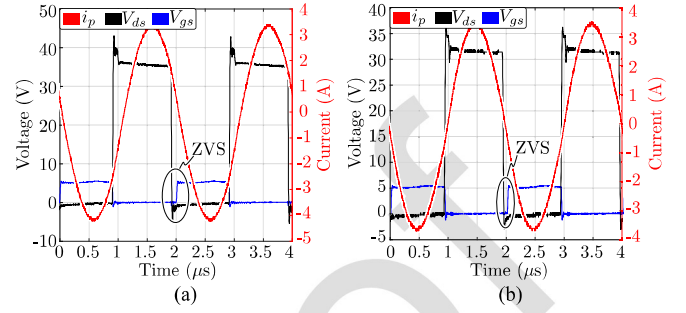


Fig. 12. Drain-to-source voltage,  $V_{ds}$ , gate-to-source voltage,  $V_{gs}$ , of  $S_2$  and primary-side current,  $i_p$ , when (a) transmitter and receiver are made with conventional winding pattern and (b) one of the transmitter and receiver is made with the proposed winding pattern.

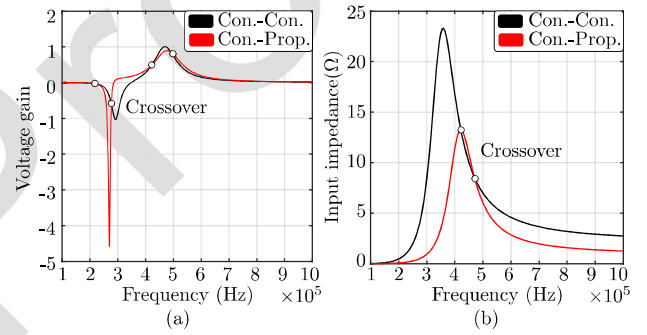


Fig. 13. Comparison between proposed winding pattern and conventional winding pattern in terms of the (a) voltage gain and (b) input impedance. [calculated based on resonant tank parameters in Fig. 11(c) with 10  $\Omega$  load resistance].

of switch  $S_2$  and primary-side current,  $i_p$ , are presented in Fig. 12. Since the  $V_{ds}$  of switch  $S_2$  decreases to zero before the high-level gate signal, the switch  $S_2$  turns ON at zero voltage.

The input impedance and voltage gain of two different cases (conventional-conventional winding pattern and conventional-proposed winding pattern) are calculated according to (17) and compared in Fig. 13 [23]

$$G_v = \frac{v_{\text{out}}}{v_{\text{in}}} = \frac{j\omega MR_L}{Z_p(Z_s + R_L) + \omega^2 M^2}$$

$$Z_{\text{in}} = \frac{\omega^2 M^2}{Z_s + R_L} + Z_p$$

$$Z_p = j\omega(L_{\text{leak},p} + M) + \frac{1}{j\omega C_p}$$

$$Z_s = j\omega(L_{\text{leak},s} + M) + \frac{1}{j\omega C_s} \quad (17)$$

where  $G_v$  is the voltage gain ratio.  $Z_{\text{in}}$  is the input impedance.  $v_{\text{in}}$  and  $v_{\text{out}}$  are the input and output voltage to the resonant tank.  $M$ ,  $L_{\text{leak},p}$ ,  $L_{\text{leak},s}$  are the mutual inductance, primary-side, and secondary-side leakage inductance.  $C_p$  and  $C_s$  are the primary-side and secondary-side compensated capacitance.  $R_L$  is the equivalent load resistance.

From Fig. 13(a), there are four crossover points at the voltage gain curve. It indicates that the same voltage gain ratio can be



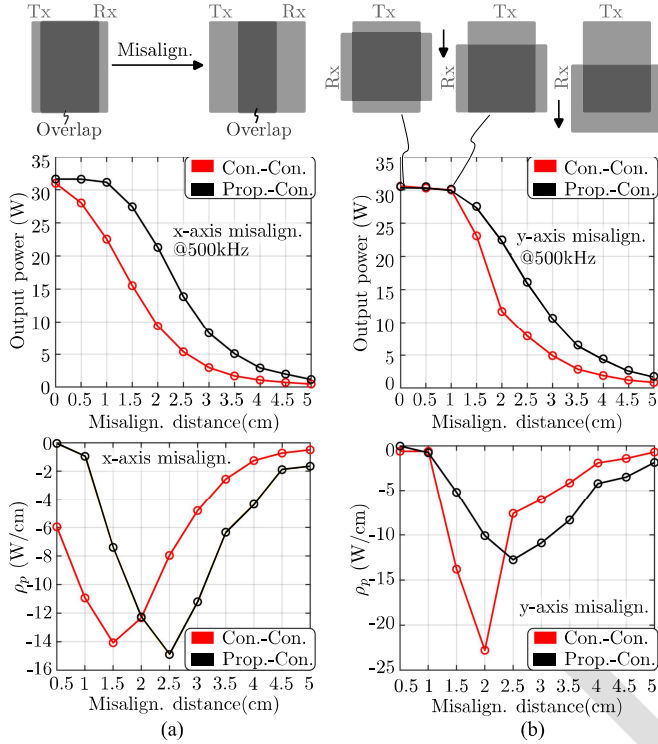


Fig. 14. Output power variation and its gradient with (a) x-axis misalignment and (b) y-axis misalignment.

obtained with different mutual inductance values. In Fig. 13(b), there are two crossover points at the input impedance curve at which the same input impedance can be obtained. According to (18), the same amount of power can be transmitted with nearly the same current amplitude

$$P_{\text{out}} = I^2 Z_{\text{in}} \quad (18)$$

where  $P_{\text{out}}$  is the output power. From Fig. 12, the current amplitude for the conventional-conventional winding pattern case is 3.26 A, and for conventional-proposed winding pattern is 3.28 A. The difference between them is 20 mA for transferring the same amount of power.

The input power and output power are measured with PM100 single-phase power analyzer. The misalignment test is conducted on the x-axis and y-axis separately, and the resulting output power variation is presented in Fig. 14. The output power misalignment sensitivity factor is calculated as

$$\rho_p = \left. \frac{\partial P_{\text{out}}}{\partial x} \right|_{x=x_i, y_i} \quad (19)$$

where  $\rho_p$  is the output power sensitivity factor.  $x$  is a misalignment-distance variable, and  $x_i, y_i$  are the x-axis and y-axis misalignment distance.

The resistance of transmitter and receiver coils are reduced by 115 m $\Omega$  and 32 m $\Omega$  when the transmitter is wound with the proposed winding pattern. When the x-axis and y-axis misalignment occurs, the efficiency and output power decrease with the misalignment distance. However, the overall output power of

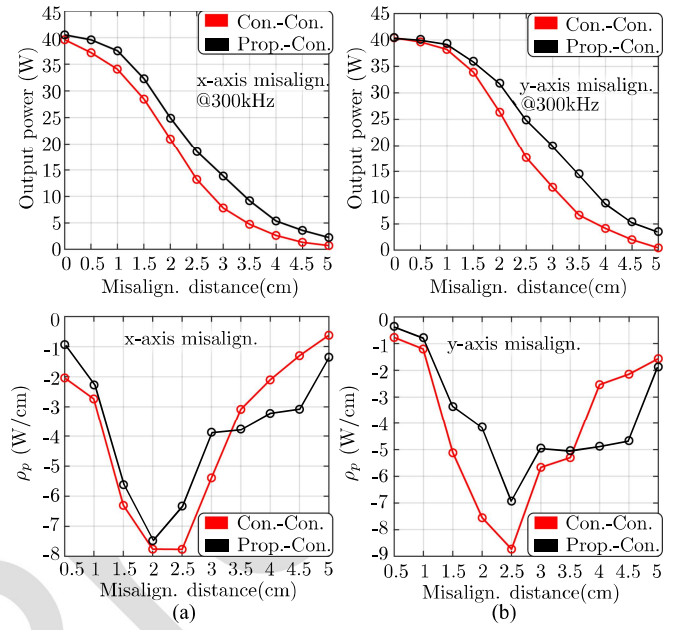


Fig. 15. Output power variation and its gradient with (a) x-axis misalignment and (b) y-axis misalignment.

the proposed winding pattern as transmitter and conventional winding pattern as the receiver is higher than the conventional winding pattern as transmitter and receiver.

The output power gradient at different misalignment distance are calculated according to (19) and presented in Figs. 14 and 15. When the misalignment distance is below 2.5 cm, the output power variation for the proposed winding pattern as transmitter and conventional winding pattern as receiver is lower than the conventional winding pattern as transmitter and receiver. The maximum output power variation is reduced by 30% at 1 cm x-axis misalignment distance, and 46% at 2 cm y-axis misalignment distance. In the y-axis misalignment setup, the transmitter and receiver are orthogonal to each other. This orientation is shown in upper subfigure in Fig. 14(b). When misalignment occurs, the overlapped area between the transmitter and receiver firstly remains unchanged. It is corresponding to the misalignment distance from 0 cm to 1 cm in Fig. 14(b). When the misalignment distance continues increasing, the overlapped area between the transmitter and receiver reduces, and the output power is reduced as well. When the misalignment distance increases above 2.5 cm, the output power decreases significantly for both cases. This is because mutual magnetic flux is significantly reduced when the large misalignment occurs. A another test is conducted on 300 kHz according to Qi standard as shown in Fig. 15. The proposed winding pattern improves the misalignment tolerance by 29% at 2 cm when x-axis misalignment occurs, and 41% at 2.5 cm when y-axis misalignment occurs.

#### IV. CONCLUSION

This study presents a misalignment-tolerant winding pattern and its design method. It alternates the winding direction to

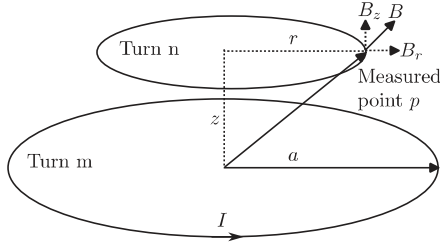


Fig. 16. Magnetic field density decomposition at measured point p due to the current-carrying conductor turn m [19].

create a semihomogeneous magnetic field. Since the transmitter and receiver magnetic field intensity variation is reduced, the coil misalignment tolerance is improved. As the reversed winding position affects the misalignment tolerance, ac resistance, inductance, and coupling factor, a design method is proposed in this study to find the suitable reversed winding position. From the design result, there was a tradeoff between the misalignment tolerance and system efficiency. High misalignment tolerant coil might result in the efficiency reduction, and high efficient coil design might result in low misalignment tolerance. Four coils were designed with maximally 88% ac resistance reduction at 2 MHz under the same coil geometry, wire type, and length. The misalignment tolerance is validated on a 30-W demo with maximally 46% output power variation reduction.

However, the proposed winding pattern reduces the mutual inductance and coupling factor at aligned condition, which limited the power transfer distance for proposed coil structure. One of the future works is to improve the transmission distance and maintain high misalignment tolerance.

## APPENDIX

For circular filament shown in Fig. 16, the magnetic field density at the radial and axial directions are calculated by

$$\begin{aligned} B_{pr} &= B_0 \frac{\gamma}{\pi \sqrt{Q}} \left[ E(k) \frac{1 + \alpha^2 + \beta^2}{Q - 4\alpha} - K(k) \right] \\ B_{pz} &= B_0 \frac{1}{\pi \sqrt{Q}} \left[ E(k) \frac{1 - \alpha^2 - \beta^2}{Q - 4\alpha} + K(k) \right] \end{aligned} \quad (20)$$

where  $E(k)$ ,  $K(k)$  are the complete elliptic integral functions in first and second kind. Referring Fig. 16  $H_0$ ,  $\alpha$ ,  $\beta$ ,  $\gamma$ ,  $Q$ , and  $k$  are as follows:

$$B_0 = I\mu_0/(2a)$$

$$Q = [(1 + \alpha)^2 + \beta^2]$$

$$k = \sqrt{\frac{4\alpha}{Q}}$$

$$\alpha = \frac{r}{a}$$

$$\beta = \frac{z}{a}$$

$$\gamma = \frac{z}{r}$$

where  $a$ ,  $I$  are the radius and peak current of turn m.  $r$ ,  $z$  are the distance in radial and axial directions between center of turn m and the measurement point of turn n. The radial and axial magnetic field intensity components at measured point p are obtained

$$\begin{aligned} H_{pr} &= \frac{B_{pr}}{\mu_0} = I\mathcal{H}_{pr} \\ H_{pz} &= \frac{B_{pz}}{\mu_0} = I\mathcal{H}_{pz} \end{aligned} \quad (21)$$

where  $\mathcal{H}_{pr}$ ,  $\mathcal{H}_{pz}$  are the unit magnetic field intensity on axial and radial directions. The proximity-effect power loss is

$$P_{prox} = I^2 G_r \iint_{s_i} \mathcal{H}_{pr}^2 + \mathcal{H}_{pz}^2 ds. \quad (22)$$

The proximity-effect resistance is

$$R_{prox} = 2G_r \iint_{s_i} \mathcal{H}_{pr}^2 + \mathcal{H}_{pz}^2 ds. \quad (23)$$

## ACKNOWLEDGMENT

The authors acknowledge the suggestions and comments provided by the reviewers and editors. The authors acknowledge the help and suggestions from Shaokang, Zhixing, and Hackl Herbert.

## REFERENCES

- [1] R. Bosshard, J. W. Kolar, J. Mhlethaler, I. Stevanovi, B. Wunsch, and F. Canales, "Modeling and  $\eta$  -  $\alpha$  - Pareto optimization of inductive power transfer coils for electric vehicles," *IEEE Trans. Emerg. Sel. Topics Power Electron.*, vol. 3, no. 1, pp. 50–64, Mar. 2015.
- [2] R. Link, "Resonant link product page," Accessed: Mar. 29, 2023. [Online]. Available: <https://www.resonant-link.com/>
- [3] O. Knecht, R. Bosshard, and J. W. Kolar, "High-efficiency transcutaneous energy transfer for implantable mechanical heart support systems," *IEEE Trans. Power Electron.*, vol. 30, no. 11, pp. 6221–6236, Nov. 2015.
- [4] S. Kim et al., "Thermal evaluation of an inductive power transfer pad for charging electric vehicles," *IEEE Trans. Indust. Electron.*, vol. 69, no. 1, pp. 314–322, Jan. 2022.
- [5] S. Jayalath and A. Khan, "Design, challenges, and trends of inductive power transfer couplers for electric vehicles: A review," *IEEE Trans. Emerg. Sel. Topics Power Electron.*, vol. 9, no. 5, pp. 6196–6218, Oct. 2021.
- [6] "Wireless power transfer for light-duty plug-in/electric vehicles and alignment methodology," *SAE International Std.*, 2022. [Online]. Available: [https://www.keysight.com/us/en/assets/7018-04256/data\\_sheets/5991-3890.pdf](https://www.keysight.com/us/en/assets/7018-04256/data_sheets/5991-3890.pdf)
- [7] Y. Chen, R. Mai, Y. Zhang, M. Li, and Z. He, "Improving misalignment tolerance for IPT system using a third-coil," *IEEE Trans. Power Electron.*, vol. 34, no. 4, pp. 3009–3013, Apr. 2019.
- [8] Y. Yao, Y. Wang, X. Liu, Y. Pei, and D. Xu, "A novel unsymmetrical coupling structure based on concentrated magnetic flux for high-misalignment IPT applications," *IEEE Trans. Power Electron.*, vol. 34, no. 4, pp. 3110–3123, Apr. 2019.
- [9] G. A. J. Elliott, S. Raabe, G. A. Covic, and J. T. Boys, "Multiphase pickups for large lateral tolerance contactless power-transfer systems," *IEEE Trans. Ind. Electron.*, vol. 57, no. 5, pp. 1590–1598, May 2010.
- [10] F. Wen, X. Cheng, Q. Li, W. Zhao, X. Zhu, and Y. Wu, "A strong misalignment tolerance dual-channel coupler for wireless power transfer system," *IEEE Trans. Appl. Supercond.*, vol. 31, no. 8, pp. 1–5, Nov. 2021.
- [11] M. Budhia, J. T. Boys, G. A. Covic, and C.-Y. Huang, "Development of a single-sided flux magnetic coupler for electric vehicle IPT charging systems," *IEEE Trans. Indust. Electron.*, vol. 60, no. 1, pp. 318–328, Jan. 2013.

- [12] T.-S. Lee, S.-J. Huang, S.-H. Dai, and J.-L. Su, "Design of misalignment-insensitive inductive power transfer via interoperable coil module and dynamic power control," *IEEE Trans. Power Electron.*, vol. 35, no. 9, pp. 9024–9033, Sep. 2020.
- [13] Y. Zhang, S. Chen, X. Li, and Y. Tang, "Design methodology of free-positioning nonoverlapping wireless charging for consumer electronics based on antiparallel windings," *IEEE Trans. Ind. Electron.*, vol. 69, no. 1, pp. 825–834, Jan. 2022.
- [14] P. Zhang, M. Saeedifard, O. C. Onar, Q. Yang, and C. Cai, "A field enhancement integration method featuring misalignment tolerance for wireless EV charging using LCL topology," *IEEE Trans. Power Electron.*, vol. 36, no. 4, pp. 3852–3867, Apr. 2021.
- [15] Z. Yuan, M. Saeedifard, C. Cai, Q. Yang, P. Zhang, and H. Lin, "A misalignment tolerant design for a dual-coupled LCC-S-compensated WPT system with load-independent CC output," *IEEE Trans. Power Electron.*, vol. 37, no. 6, pp. 7480–7492, Jun. 2022.
- [16] Q. Wang, W. Che, M. Mongiardo, and G. Monti, "Wireless power transfer system with high misalignment tolerance for bio-medical implants," *IEEE Trans. Circuits Syst. II*, vol. 67, no. 12, pp. 3023–3027, Dec. 2020.
- [17] Q. Xu, Q. Hu, H. Wang, Z.-H. Mao, and M. Sun, "Optimal design of planar spiral coil for uniform magnetic field to wirelessly power position-free targets," *IEEE Trans. Magn.*, vol. 57, no. 2, pp. 1–9, Feb. 2021.
- [18] J. Ferreira, "Improved analytical modeling of conductive losses in magnetic components," *IEEE Trans. Power Electron.*, vol. 9, no. 1, pp. 127–131, Jan. 1994.
- [19] M. Lu and K. D. T. Ngo, "Analytical calculation of proximity-effect resistance for planar coil with litz wire and ferrite plate in inductive power transfer," *IEEE Trans. Ind. Appl.*, vol. 55, no. 3, pp. 2984–2991, May/Jun. 2019.
- [20] KEYSIGHT, "Datasheet of E4990 a impedance analyzer," Accessed: Jan. 10, 2023.
- [21] K. Jensen, "Litz wire practical design consideration for today's high frequency application," Accessed: Jun. 06, 2023. [Online]. Available: <https://www.psma.com/sites/default/files/uploads/files/Litz%20Wire%20Practical%20Design%20Considerations%20for%20Today's%20HF%20Applications%20Jensen%2C%20Rubadue.pdf>
- [22] E. T. S. Institute, "TR 103 493 - V1.1.1 - system reference document (SRdoc): wireless power transmission (WPT) systems operating below 30 MHz," Accessed: Apr. 12, 2023. [Online]. Available: [https://www.etsi.org/deliver/etsi\\_tr/103400\\_103499/103493/01\\_01\\_01\\_60/tr\\_103493v010101p.pdf](https://www.etsi.org/deliver/etsi_tr/103400_103499/103493/01_01_01_60/tr_103493v010101p.pdf)
- [23] W. Zhang, S.-C. Wong, C. k. Tse, and Q. Chen, "Design for efficiency optimization and voltage controllability of series-series compensated inductive power transfer systems," *IEEE Trans. Power Electron.*, vol. 29, no. 1, pp. 191–200, Jan. 2014.



**Weihao Zhao** received the M.S. degree in power electronics and drives from Aalborg University, Aalborg, Denmark, in 2022.

His research interests include inductive power transfer and design optimization.



**Zhan Shen** (Member, IEEE) received the B.E. degree in electrical engineering and automation from the Nanjing University of Aeronautics and Astronautics, the M.E. degree in electrical engineering from Southeast University, Nanjing, China, in 2013 and 2016, respectively, and the Ph.D. degree in energy technology from Aalborg University, Aalborg, Denmark, in 2020.

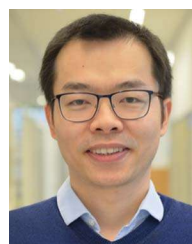
He is currently an Associate Professor with Southeast University. He was a Visiting Scholar with the RWTH Aachen University, Aachen, Germany, and with the Massachusetts Institute of Technology (MIT), Cambridge, MA, USA. In 2016, he was with the ABB Corporate Research Center, Beijing, China. His research interests include power electronic system integration, magnetic components, and artificial intelligence.

Dr. Shen was the recipient of multiple Best Paper and Best Presenter Awards of the IEEE PELS sponsored conferences, and the Outstanding Reviewer Award of the IEEE TRANSACTIONS ON POWER ELECTRONICS.



**Yingzhou Peng** (Member, IEEE) received the B.S. degree in electrical engineering from Harbin Engineering University, Harbin, China, in 2014, the M.S. degree in power electronics from Chongqing University, Chongqing, China, in 2017, and the Ph.D. degree in power electronics from Aalborg University, Aalborg, Denmark, in 2020.

He is currently an Assistant Professor with Hunan University, Changsha, China. In 2020, he was a Visiting Researcher with the Electrical Power and Energy Conversion Lab, Cambridge University, Cambridge, U.K. His research interests include the failure mechanisms analysis of power electronic components, and the improvement of the robustness and reliability of power converters by means of condition monitoring.



**Huai Wang** (Senior Member, IEEE) received the B.E. degree in electrical engineering from the Huazhong University of Science and Technology, Wuhan, China, in 2007, and the Ph.D. degree in power electronics from the City University of Hong Kong, Hong Kong, in 2012.

He is currently a Professor with AAU Energy, Aalborg University, Aalborg, Denmark, where he leads the group of Reliability of Power Electronic Converters (ReliaPEC) and the mission on Digital Transformation and AI. From August to September 2014, he was a Visiting Scientist with the ETH Zurich, Switzerland. From September to November 2013, he was with the Massachusetts Institute of Technology (MIT), Cambridge, MA, USA. In 2009, he was with the ABB Corporate Research Center, Switzerland. His research interests include the fundamental challenges in modeling and validating power electronic component failure mechanisms and application issues in system-level predictability, condition monitoring, circuit architecture, and robustness design.

Dr. Wang received the Richard M. Bass Outstanding Young Power Electronics Engineer Award from the *IEEE Power Electronics Society* in 2016 and the 1st Prize Paper Award from *IEEE TRANSACTIONS ON POWER ELECTRONICS* in 2021. He serves as an Associate Editor for *Journal of Emerging and Selected Topics in Power Electronics* and *IEEE TRANSACTIONS ON POWER ELECTRONICS*. He was elected as a Member of the Danish Academy of Technical Sciences in 2023.